JGR Earth Surface

Key Points:
- Opportunistic use of tidewater glacier terminus lidar data combined with numerical plume model
- No evidence that plume surfacing increases major calving event frequency; plumes are associated with longer delays between calving
- Direct plume-driven mass loss at deep tidewater glaciers may be much less than calving mass loss, in contrast to shallower termini

Supporting Information:
- Supporting Information S1

Correspondence to:
A. Everett,
alistair.everett@met.no

The Impacts of a Subglacial Discharge Plume on Calving, Submarine Melting, and Mélange Mass Loss at Helheim Glacier, South East Greenland

Alistair Everett[1,2] , Tavi Murray[2] , Nick Selmes[2,3] , David Holland[4] , and Dominic E. Reeve[5]

[1]Norwegian Meteorological Institute, Tromsø, Norway, [2]Glaciology Group, College of Science, Swansea University, Swansea, UK, [3]Plymouth Marine Laboratory, Plymouth, UK, [4]Center for Atmosphere Ocean Science, Courant Institute of Mathematical Sciences, New York University, New York, NY, USA, [5]Energy & Environment Group, College of Engineering, Swansea University, Swansea, UK

Abstract Almost half of the Greenland ice sheet's mass loss occurs through iceberg calving at marine terminating glaciers. The presence of buoyant subglacial discharge plumes at these marine termini are thought to increase mass loss both through submarine melting and by undercutting that consequently increases calving rates. Plume models are used to predict submarine melting and undercutting. However, there are few observations that allow these relationships to be tested. Here, we use airborne lidar from the terminus of Helheim Glacier, SE Greenland to measure the bulge induced at the surface by the upwelling plume. We use these measurements to estimate plume discharge rates using a high-resolution, three-dimensional plume model. Multiyear observations of the plume are compared to a record of calving from camera and icequake data. We find no evidence to suggest that the presence of a plume, determined by its visibility at the surface, increases the frequency of major calving events and also show that mass loss at the terminus driven directly by plume discharge is significantly less than mass loss from major calving events. The results suggest that the contribution of direct plume-driven mass loss at deep marine-terminating glaciers may be less than at shallower termini.

Plain Language Summary A major uncertainty in how much ice is lost from the Greenland and Antarctic ice sheets is how changes in the ocean can affect melting and ice loss from glaciers flowing into the ocean. Previous studies have found links between ocean properties and the advance and retreat of glaciers. In our study, we use new observations to examine some of the processes which might cause this. We look at plumes of meltwater which are released from glaciers deep below the water surface. As this meltwater rises it pulls in water from the surrounding fjord; affecting circulation and melting the ice faster. We use cameras to make a timeline of when these plumes reach the surface and when large pieces of ice, some many kilometers across, detach from the glacier in calving events. Our data shows that large calving events do not consistently happen after plume activity. We use a model of the plume to estimate melt rates and we find that ice loss caused directly by the plume is much less than that caused by large calving events. Our results show that we should study processes at the ice-ocean interface in detail to better understand how the ocean affects glaciers.

1. Introduction

The response of marine-terminating glaciers to oceanic forcing is one of the major unknowns in predicting the future response of the Greenland ice sheet to climate change (Church et al., 2013). One of the key reasons for this uncertainty is our limited understanding of processes occurring in the ice-ocean boundary layer (Straneo & Cenedese, 2015). In this region, processes on the order of meters and centimeters drive melt rates which influence larger-scale processes such as calving, ice dynamics, and fjord circulation (Carroll et al., 2015; Holland et al., 2008; O'Leary & Christoffersen, 2013; Slater et al., 2017b; Straneo & Heimbach, 2013). Hence, these processes potentially have significant implications for the future stability of large marine-terminating outlet glaciers and the ice sheets they drain.

The difficulties in understanding the ice-ocean boundary layer stem from both the small-scale nature of the dynamics, which are difficult to include in large-scale ice and ocean models, and the inaccessible and

hazardous nature of the environment, which make access and data collection both costly and dangerous. One of the main features of this environment which has received considerable attention in recent years are the buoyant plumes of subglacial discharge which are frequently observed at the front of marine-terminating glaciers (e.g., Carroll et al., 2016; Mankoff et al., 2016; Motyka et al., 2013; Schild et al., 2016; Slater et al., 2017a; Xu et al., 2013). These plumes are driven by the release of subglacial discharge from the bed of the glacier and have been shown to significantly amplify melt rates on the ice front both directly (Jenkins, 2011; Motyka et al., 2013) and indirectly through effects on fjord circulation (Slater et al., 2018). The increased melt rates have been theorized to influence calving through undercutting of the terminus, leading to collapse of the unsupported ice above, and also through complex effects on the near terminus stress field (Benn et al., 2017; O'Leary & Christoffersen, 2013). However, detailed studies of the links between plumes and calving events are limited. Recent observations at Tunabreen, a relatively shallow tidewater glacier in Svalbard with a terminus depth of around 30–50 m, showed a higher frequency of undercut and collapse calving events in areas of plume activity (How et al., 2019). However, at deeper tidewater glaciers around the coast of Greenland different mechanisms, such as buoyant flexure (Benn et al., 2007; James et al., 2014), can lead to much larger calving events. The relationship between submarine melting and these major calving events is more complex and modeling studies have shown the potential for both amplification and suppression of calving (Benn et al., 2017; Ma & Bassis, 2019; O'Leary & Christoffersen, 2013).

Major advances have been made in recent years in modeling and parameterizing plumes and the melt rates which they drive at the terminus (e.g., Carroll et al., 2016; Jenkins, 2011; Mankoff et al., 2016; Slater et al., 2016; Xu et al., 2013); however, a number of challenges remain. One of the key difficulties is comparing these model results to observational data, primarily due to the difficulties in collecting such data. Recently, a number of studies have begun to address this. Short- and long-term observations of the plume area on the fjord surface have been made at glaciers on the west coast of Greenland (Schild et al., 2016; Slater et al., 2017a) and in Svalbard (How et al., 2017). This form of observation is limited to glaciers without a significant ice mélange at the terminus and, as yet, there is no reliable way to convert these observations into estimates of discharge volume in the plume, which is one of the critical factors for determining the melt rate on the terminus. Other indirect methods to measure plumes have used seismometers to monitor variations in subglacial discharge (Bartholomaus et al., 2015) or oceanographic sections to deduce plume properties (Jackson et al., 2017). Perhaps most significantly, direct measurements were collected from within a plume on the west coast of Greenland by Mankoff et al. (2016) and, following this, Sutherland et al. (2019) successfully measured submarine melting at an Alaskan glacier. The latter study noted that in plume-driven melt regions their observations were broadly consistent with the theory. Few plume studies exist for glaciers with a thick ice mélange, however, due to the further complications in accessing and observing the plume, meaning that the influence of plumes on mélange has received little, if any, attention.

This study focusses on Helheim Glacier; one of the largest marine-terminating outlets of the Greenland ice sheet with a terminus depth between 500 and 700 m deep (Enderlin et al., 2014; Joughin et al., 2008; Kehrl et al., 2017). We build upon previous work by presenting a detailed, multiyear observational and modeling study of the influence of a plume driven by subglacial discharge on both the terminus and mélange melt rates and calving activity at Helheim Glacier. We combine a high-resolution plume model with a record of plume activity on the surface of the fjord and calving events derived from cameras and glacial earthquake monitoring. High-resolution LiDAR data reveal the surface profile of the turbulent bulge where the plume reaches the surface, allowing a comparison between modeled and observed plume dynamics. The plume observations are compared with a record of calving activity in an attempt to identify whether the plume can be linked to an increased rate of calving at Helheim glacier.

2. Methods

2.1. High-Resolution Plume Modeling

The plume model used here is based on Fluidity (Piggott et al., 2008), an open-source, finite element fluid dynamics code. Fluidity can be run using a mesh which is fully unstructured in three dimensions. This allows high mesh resolution to be focused in discrete locations within the domain, for example close to the subglacial discharge outlet, without unnecessarily high resolutions in other areas of the domain. Fluidity also has the ability to solve equations on a time-evolving mesh (Davies et al., 2011), and therefore presents

opportunities for future developments to model a time-evolving ice front in three dimensions, though this has not been investigated in this study. Fluidity has previously been used by Kimura et al. (2013, 2014) to model plumes of subglacial discharge; the setup used here builds upon their work but differs in the choice of discretization and handling of subgrid-scale turbulence.

Our setup uses fluidity to solve the incompressible, nonhydrostatic, Boussinesq form of the momentum and continuity equations in combination with an incompressible form of the advection-diffusion equations for temperature and salinity. The equations are closed with the Padé ocean equation of state (McDougall et al., 2003). The equations are discretized in space using a first-order continuous Galerkin discretization for velocity and pressure (a P_1P_1 element pair). We also use a second-order continuous Galerkin discretization for a balanced pressure solve, which is necessary in a P_1P_1 element pair (see AMCG [2015]). A first-order control volume discretization is used for temperature and salinity.

To parameterize the turbulent processes below the mesh resolution, we use a large eddy simulation (LES) turbulence model with a Smagorinsky-Lilly subgrid model (Bull et al., 2012; Smagorinsky, 1963). The Smagorinsky-Lilly model uses a characteristic length scale, the strain rate tensor, and an empirical Smagorinsky coefficient to calculate a spatially and temporally varying eddy viscosity. This eddy viscosity is then included in the viscous stress tensor in the momentum equation. The LES turbulence model comes with some increase in computational expense when compared to other models which calibrate the diffusivity (e.g., Kimura et al., 2014; Slater et al., 2015), but minimizes the impact of the spatially varying mesh resolution on the model dynamics and relates the subgrid processes to the flow field properties more closely.

The model domain is a semicylindrical mesh with a radius of 200 m, where the flat face represents the ice front and the cylindrical face represents the boundary with the fjord. Due to uncertainty about the depth of the ice front, two depths of 500 and 700 m were tested. The mesh resolution is 1 m at the center of the ice front and decreases radially to 20 m at the fjord boundaries. Close to the inlet, the mesh is further refined to a resolution of 0.5 m. The model is initialized with temperature and salinity profiles collected from Sermilik fjord during August 2013 (see Text S1 in the supporting information). The profiles are stratified, with warmer, more saline water at depth and colder, fresher water at the surface. The same profiles are imposed on the open boundaries of the model. The limited width of the model domain means that in this study we only consider direct mass loss by the plume, other effects on fjord circulation and wider currents which may drive melting across the ice front are not considered here.

We use the three-equation model (Holland & Jenkins, 1999) to calculate melt rates on the ice-front, implemented in Fluidity by Kimura et al. (2014). The equations are used in the form

$$m'L + m'c_I(T_b - T_I) = c_0 u_\infty \gamma_T (T_\infty - T_b),\tag{1}$$

$$m'S_b = u_\infty \gamma_S (S_\infty - S_b),\tag{2}$$

$$T_b = aS_b + b + cP,\tag{3}$$

where parameters with the ∞ subscript are calculated in the plume model and the remaining constants and variables are listed in Table S1. We also apply a background velocity of 10^{-4} ms^{-1} to simulate melt in the absence of convection (McConnochie & Kerr, 2017).

A horizontally facing inlet at the foot of the ice boundary is used to release subglacial discharge into the domain. The channel is assumed to be semicircular and we follow Slater et al. (2015) in using the relationship of Schoof (2010) to relate discharge to channel velocity and cross-sectional area. To produce fully turbulent conditions at the inlet we use the synthetic eddy method (SEM) (Jarrin et al., 2006). When used with an LES turbulence model, the SEM inlet produces a more rapid transition to turbulent flow, and therefore more realistic plume behavior, than a uniform velocity at the inlet (Keating et al., 2004).

LiDAR measurements, described below, provide measurements of the ocean surface height over the plume; for comparison, we therefore extract the surface height η from the model results by extracting the perturbation pressure p' from the surface of the model and using the relationship $p' = \rho g \eta$. Then, for each surface height field, a characteristic peak height is calculated as the mean of the top 20% of surface heights. This
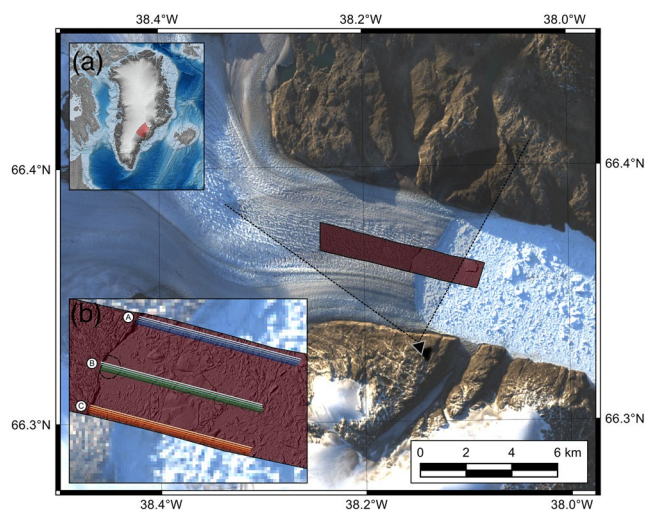
Figure 1. LiDAR swath (dark red) and camera location (black triangle with field of view shaded) at the terminus of Helheim Glacier. Inset (a) shows Helheim catchment and the location on the south east Greenland coast. Inset (b) shows a magnified view of the LiDAR swath and profiles A, B, and C extracted from the LiDAR data. In the inset image, the dashed black line adjacent to (B) indicates the extent of the opening in the mélange formed by the plume at the time the LiDAR was collected. The background is a Landsat 8 image from July 8, 2014.

lessens the impact of extreme outliers in surface height point measurements. The data are then presented as the temporal mean and standard deviation of characteristic surface heights calculated during the model run.

2.2. Landsat Imagery

Landsat 7 and 8 imagery, acquired from the US Geological Survey using the LandsatLook Viewer, were used to identify the presence of the plume at the fjord surface. Images were gathered covering the years 2010 through to 2014. The plume was identified in 10 images; four each from 2012 to 2014, and one each from 2010 to 2013. The plume was not visible in any of the imagery during 2011. The ice front and plume outline were manually digitized from the available images. The area of the plume was derived from these outlines; however, these area estimates have a large associated uncertainty as the size of the plume is often close to the 30 m resolution of the imagery, and can also be obscured due to the scanline correction error which affects Landsat 7 imagery. The magnitude of the error in digitizing the area was approximated by allowing the extent of the plume to vary by ±30 m (i.e., 1 pixel width) and using the minimum and maximum areas as conservative upper and lower bounds on the area.

2.3. Terminus Cameras and Glacial Earthquake Record

Two cameras have collected images from the terminus of Helheim Glacier between 2008 and 2014. In combination, these cameras cover the full width of the ice front with small blind spots close to the margins where rock obscures the view. The cameras collect images once every hour, providing a high temporal-resolution record of terminus behavior. Camera images collected between 1st June and 30th September in each year were used to manually identify major calving events and times when the plume was visible on the surface of the fjord through the mélange. Images outside this period were also examined, but no evidence of plume activity was found. The record was created with a daily resolution, and the presence of the plume was only recorded if it was clearly visible in multiple images within one day. It is important to stress here that we only identify the plume at the surface, and that the plume may persist for longer periods without surfacing. To address this, we also consider melt rates of nonsurfacing plumes in our modeling results.

Example camera images are included in Figure S2 to illustrate how calving events and the plume were identified. Major calving events referred to throughout this paper are those which affected more than −25% of the terminus visible in the images. These major calving events are characteristic of deep Greenlandic glaciers and do not occur frequently at shallow tidewater glaciers, such as those in Svalbard.

There are a number of gaps in the data during the summer months; particularly in 2011, when no images were collected until 31 July. To cover these periods, the camera-derived calving record was supplemented with a record of glacial earthquakes which is available for 1993–2013 (Olsen & Nettles, 2017; Tsai & Ekström, 2007; Veitch & Nettles, 2012).

2.4. Hyperspectral and LiDAR Data

Hyperspectral and LiDAR data were collected over the terminus of Helheim glacier on July 17, 2013 by the Natural Environment Research Council (NERC) Airborne Research & Survey Facility (ARSF) flight IG13/21 (Figure 1). Hyperspectral data were collected using a Specim Eagle SN110001 Hyperspectral Sensor and LiDAR data were collected using a Leica ALS50-II Airborne Laser Scanner. The 1.1-km-wide swath captured the surface height of the mélange close to the terminus of the glacier, and coincided with the presence of a plume that created an opening in the mélange immediately in front of the terminus. The high

turbidity and turbulence of the water surface where the plume emerged provided sufficient backscatter for the LiDAR system to measure the surface height of the water.

Both the hyperspectral and LiDAR data were processed to Level 1B by the ARSF. The hyperspectral data were provided as a 3 × 3 m resolution georeferenced raster image with imagery over 252 bands in the visible to near-infrared spectrum. The LiDAR data were provided as a quality-controlled LiDAR point cloud with a resolution of ∼2.2 m in the scan direction and ∼1.2 m in the flight direction with a mean error in the vertical of 4.9 cm. The LiDAR point cloud data were then further filtered to remove any remaining atmospheric returns and spurious data points by discarding any points with a height more than 200 m above sea level. The water surface over the plume was extracted from surrounding data by manually digitizing the water extent from the hyperspectral imagery. The remaining LiDAR point cloud data were then interpolated onto a uniform 2 × 2 m grid using a triangulated irregular networks algorithm and smoothed using a Gaussian filter to reduce noise.

2.4.1. Ice Front

The hyperspectral and LiDAR data also captured an embayment in the ice front behind the plume. The size of this embayment was used to estimate the melt rate of the terminus driven by the plume at the surface. To measure the retreat of the embayment, a line was interpolated across the embayment in line with the ice front on either side. The perpendicular distance between the interpolated ice front and the observed ice front in the hyperspectral images was measured at 10 m intervals along the assumed ice front and taken to represent the total retreat driven by the plume. The total retreat was converted into a retreat rate by dividing it by the time which the plume was visible at the ice front, as derived in the plume record.

Estimating the melt rate in this way gives an average retreat rate during the time the plume had been present at the surface, but cannot be used to infer details about fluctuations in discharge volume and plume properties during this time. The method assumes that the melt rate outside the embayment is small relative to that within the plume, and removes the requirement for any knowledge about the velocity of the ice at the terminus. As there were no previous occurrences of a plume in 2013, and a large calving event occurred 7 days before the appearance of the plume, it is reasonable to assume that the ice front would have been relatively straight across the section considered in the absence of a plume. This assumption is supported by the imagery presented in Figure 1. A conservative lower bound on the plume-driven surface retreat was also estimated by extending the plume period to include the 7 days between the calving event and the plume's appearance.

2.4.2. Mélange

To quantify the impacts of the plume on the mélange, surface elevation profiles were extracted from the LiDAR data, the profiles used are illustrated in Figure 1b. The profiles were extracted by identifying three regions A, B, and C; where A and C represent areas which were not strongly affected by the plume and B represents the area directly affected by the plume. Five profiles were extracted from each region with a spacing of 10 m between profiles. Each profile was extracted from the full length of the LiDAR swath and smoothed with a 10 m moving average. The ice front was picked automatically within the profiles by identifying the maximum gradient in the surface height. The front position was then used to normalize the profiles and any data upglacier of the terminus or more than 1,600 m downfjord of the terminus were discarded.

The five normalized profiles were then averaged within each region to give three representative surface height profiles, one from either side of the plume (A and C), and another from across the plume (B). Mean surface heights were taken from each representative profile for $x > 800$ m and $x < 800$ m, where x is the distance from the ice front, allowing the mélange close to the plume to be compared to that further away. Any heights greater than 10 m were ignored in calculating the along-profile means, thereby excluding large icebergs which can dominate over the relatively short distances considered. The surface heights were converted to a mélange thickness by taking the ratio of the density of seawater in the top 50 m (temperature 1°C, salinity 30, density 1,024 kg m^{-3}) and a typical density of glacier ice (917 kg m^{-3}), suggesting that 89.5% of the ice lies below the waterline. The total thickness can therefore be approximated as 10 times the observed height above the water surface.
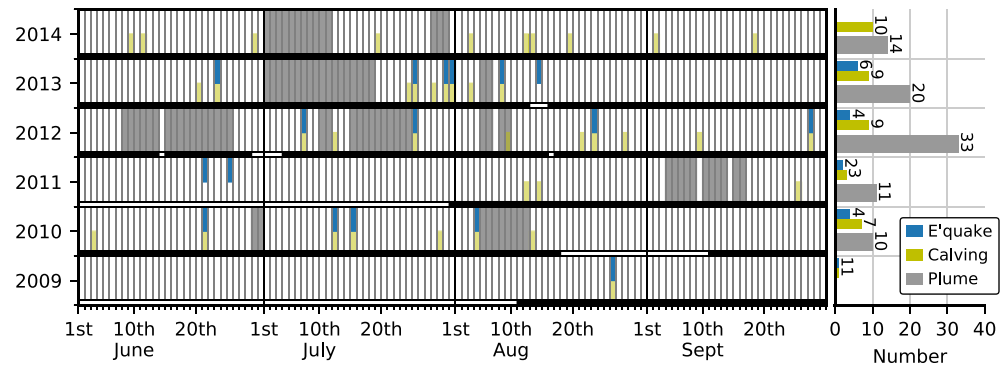
Figure 2. Digitized plume and calving record. Filled gray bars indicate a plume at the surface, yellow indicates calving identified from cameras, while blue indicates glacial earthquakes. The black/white line at the bottom of each year indicates when camera images are available (black) and not available (white). The totals during the study period are summarized to the right of the time series.

3. Results

3.1. Plume and Calving Record

The plume and calving record derived from the camera and glacial earthquake data at Helheim Glacier is shown in Figure 2. The plume was observed most frequently during 2012 when it was visible for a total of 33 days (27% of days between 1st June and 1st August). In the two other years with close to full coverage (2013 and 2014) the plume was visible for 20 and 14 days, respectively. Out of the 4 years in which images are available for 1st June to 1st August, 2012 is notable as the only year when the plume was visible before 28th June. During this period, images are missing from 14th June; however, the plume is strong and clearly visible on both 13th and 15th June, so for the remaining analysis presented here we assume that the plume is continuously surfacing from 8th to 25th June 2012, this has little overall effect on the analysis.

At Helheim Glacier, major calving events do not appear to follow the surfacing of the plume in a consistent way. Calving occurred on the same day or the day after the plume ceased to surface on four occasions, with three of these in 2012; however, on many occasions the delay was much longer. Out of the 14 periods when the plume was active at the surface, calving occurred within 1 week of the plume ceasing to surface on seven occasions, and a week or more later on four occasions. On the remaining three occasions, the plume reappeared at the surface within 2 days of disappearing without any calving occurring. A Spearman's rank test shows no significant relationship between the plume duration and the time until the next calving event ($r = 0.25$, $p = 0.45$, $n = 11$); however, the sample size available is relatively small.

Calving takes place almost continuously throughout the record with gaps between calving events as short as a few hours or as long as many weeks. Figure S3 compares the length of time between calving events when the plume is and is not visible at the surface. When the plume is not visible at the surface, the mean time between calving events is 8.83 days ($n_1 = 23$); however, when the plume is surfacing, the mean time increases to 16.60 days ($n_2 = 10$). Using the Mann-Whitney U-test, this increase is statistically significant ($U = 57.5$, $n_1 = 23$, $n_2 = 10$, $P = 0.013$, one-tailed), showing that the presence of the plume at the surface coincides with longer gaps between the occurrence of calving events.
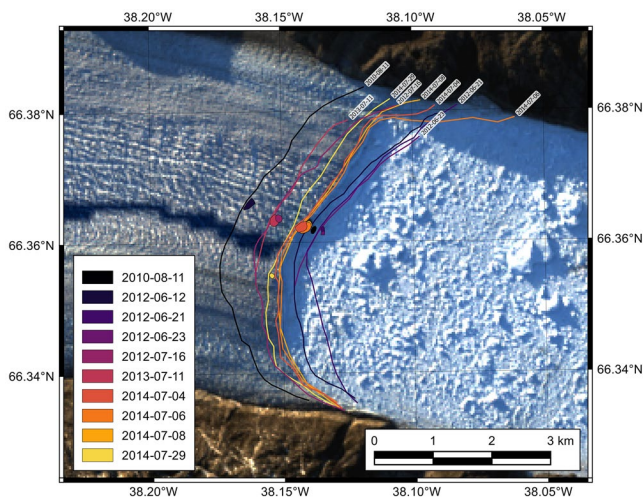

Figure 3. Plume (colored shading) and ice front positions (colored lines) for 2010–2014 digitized from Landsat imagery. Also shown as dark blue shading, entering from the western edge of the image, is the predicted path of subglacial flow (Everett et al., 2016). The background is a Landsat image from June 20, 2014.

3.2. Plume Location and Size

The digitized positions of the plume and ice front are illustrated in Figure 3 for 2010–2014. There are no available images from 2011 which
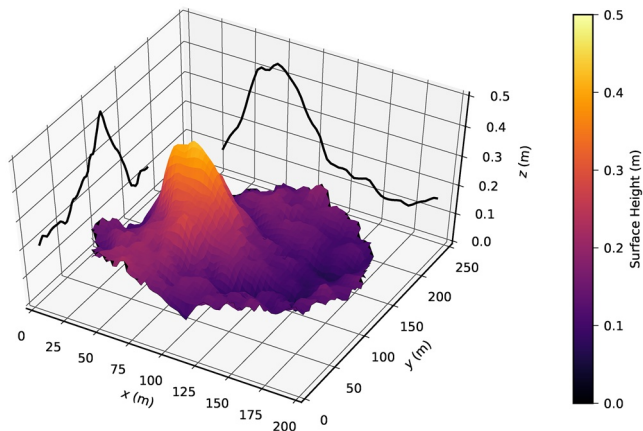
Figure 4. Three-dimensional plot of plume surface elevation from LiDAR data. Lines projected on side walls represent profiles passing through the highest point of the plume surface in the x- and y-directions, respectively. The glacier terminus is at $x = 0$. Note vertical exaggeration.

capture the plume at the surface. Between 2010 and 2014, the position of the glacier front varies by around 1.3 km; despite this large variation, the position of the plume does not vary by more than 100 m laterally across the terminus. The one exception to this is in 2014, when the plume appeared around 1 km to the south of its usual location. From the plume record, the plume persisted in this position for a relatively short period between the 28th and 31st July 2014. Earlier observations during the 2014 season showed the plume in the same location as other years. It is also notable that in all available data, only one plume is ever visible on the fjord surface at any one time.

Figure 3 illustrates the subglacial flow routing from Everett et al. (2016). This flow routing estimate gives an indication of where the outlet of the subglacial hydrological system might be expected to occur based on the hydraulic potential at the bed of the glacier. In most cases the plume positions were around 500 m north of the predicted outlet, while the anomalous position in 2014 was around 600 m to the south. Given the uncertainty in the bed elevation model and the approximations used to calculate the flow routing, the observed positions and calculated outlet position are in reasonable agreement.

In the hyperspectral and LiDAR data, the clearing in the mélange created by the plume covers an area of $36.5 \pm 1.35 \times 10^3$ m^2. The area of the plume derived from Landsat has an uncertainty of a similar magnitude to the measurement, as the plume size is close to the resolution of the imagery, and therefore it is only discussed here briefly. In Landsat data, the plume surface expression varies between 5.2×10^3 m^2 and 27.1×10^3 m^2, and is therefore consistently smaller than the area digitized from the hyperspectral data. Qualitatively it is interesting to note that, with the exception of the anomalous position in 2014, the plume area is consistently smaller in 2012 than in other years. However, three out of the four Landsat images from 2012 were collected between the 14 and 23 June, which is much earlier than the plume occurs in other years. It is therefore difficult to draw any significant conclusions from this observation.

3.3. Plume Surface Height

The LiDAR data shows that the upwelling plume formed a large bulge at the fjord surface (Figure 4). The bulge reached a maximum height of 0.46 ± 0.049 m and was tens of meters wide, dependent upon how its boundary is defined. Both the horizontal and vertical extents of the bulge were therefore significantly greater than the resolution of the LiDAR data. The volume of water contained in the bulge, above the surrounding surface, was $\sim 4.9 \times 10^3$ m^3. There is no evidence from hyperspectral data that sediment concentrations differed significantly across the plume surface, and therefore it is unlikely that the surface profile was a result of sediment concentrations in the plume affecting backscatter.

The characteristic surface height, for comparison to the modeled results, was calculated as the mean height of the top 20% of points. This gave a characteristic surface height of 0.40 m and a standard deviation of 0.02 m.

3.4. Derived Plume-Driven Melt Rates

3.4.1. Ice Front

The only plume-driven mass loss from the terminus which can be directly derived from these data is that occurring on the subaerial section of the terminus. We therefore treat this independently from submarine melting, which is much more difficult to observe. The estimated plume-driven melt rate of the terminus at the surface is shown in Figure 5, projected onto the terminus position observed in the hyperspectral image. The plume formed an embayment ~ 600 m wide, which is considerably larger than the 230 m wide opening in the mélange. The maximum plume-driven retreat is measured to be 108 m, with an average of 70.4 m
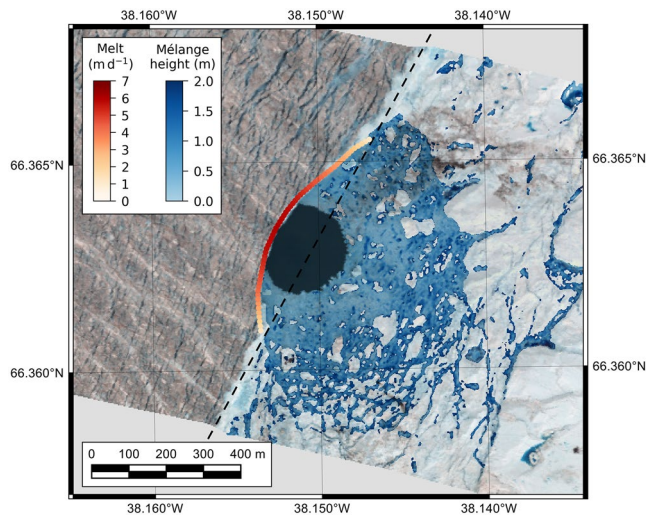
Figure 5. Hyperspectral false-color composite image with interpolated ice front position (black dashed line) and estimate of plume-driven retreat rate (white to red), see methods in Section 2.4.1. The plume is visible as an opening in the mélange. The mélange surrounding the plume below 2 m surface elevation is highlighted (light to dark blue).

across the embayment. Given that the LiDAR data show the terminus in this area to be ~70 m high, this equates to a total estimated subaerial mass loss of 3.0×10^6 m^3 of ice.

From the plume record in Figure 2, the plume had been visible for 16 days prior to the LiDAR and hyperspectral data being collected. Therefore, the time-averaged retreat rate of the ice front at center of the embayment is ~6.8 m d^{-1}, with an average of 4.4 m d^{-1} across the width of the embayment. The minimum time-averaged frontal retreat rate, estimated by extending the plume duration by 7 days to the date of the previous calving event before the plume appeared, is 4.7 m d^{-1}. This gives a frontal retreat rate in the range 4.7–6.8 m d^{-1} in the center of the embayment, with a mean in the range 3.1–4.4 m d^{-1} averaged across the embayment.

3.4.2. Mélange

Surrounding the opening in the mélange is an area where the floating ice appears to be thinner than other parts of the mélange. This indicates a region of the mélange affected by the plume which is much larger than the opening itself. This is highlighted in Figure 5 by shading the area of the mélange less than 2 m above sea level. This region reaches around 800 m across the ice front and 500 m downfjord, covering an area of ~337 × 10^3 m^2. This is significantly larger than the area of open water in the mélange cleared by the plume, which is around 230 m wide and covers 36.5 × 10^3 m^2.

The effect of the plume on the mélange can also be seen in the profiles of surface height, which are illustrated in Figure 6. For regions A and C there is a 0.3 m height difference between the mean height for
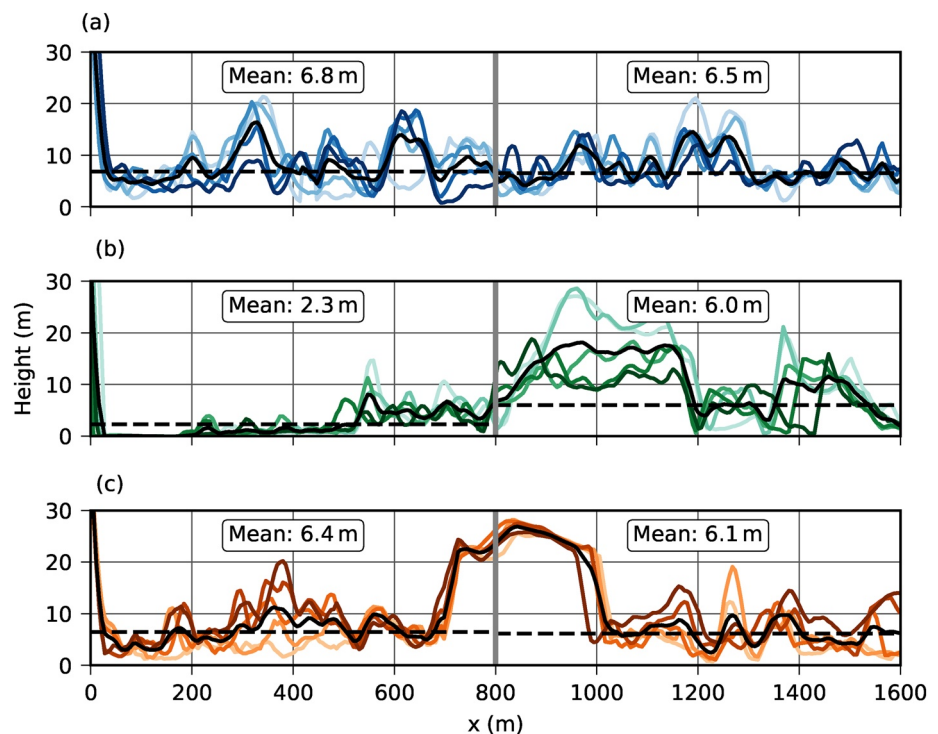

Figure 6. Mélange surface height extracted from regions A, B, and C of the LiDAR data. (a) and (c) are representative of areas away from the plume, while (b) is representative of mélange in the locality of the plume. The colors of the profiles are the same as Figure 1, and the solid black line is the average of the five profiles in each area. Dashed black lines represent the mean for $x > 800$ m and $x < 800$ m, where x is the distance from the ice front.
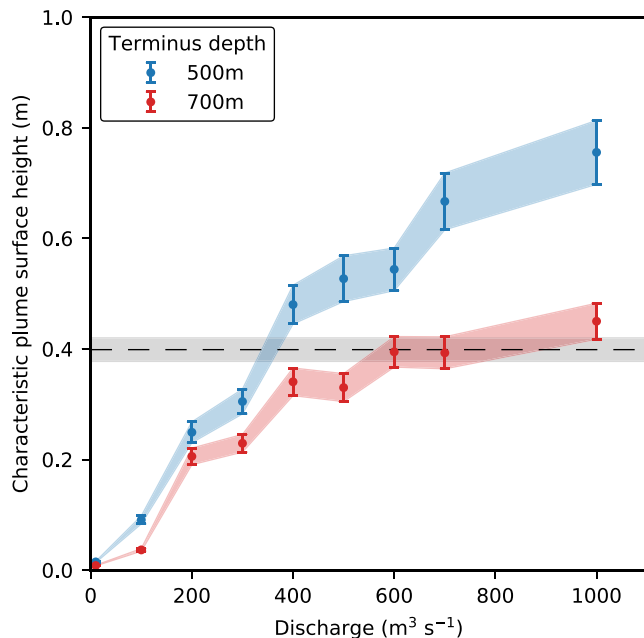
Figure 7. Characteristic plume surface heights extracted from model run with a 500 (blue) and 700 m (red) deep terminus. Solid lines represent the mean of characteristic heights observed throughout the model run, and the shaded area represents one standard deviation from the mean. The characteristic surface height extracted from the LiDAR data using the same method is also shown (black dashed line) with standard deviation (gray shade).

$x < 800$ m and $x > 800$ m, equating to a thickness difference of $\sim$3 m. In both of these cases the mélange is slightly thicker closer to the terminus. However, in region B the mean height for $x < 800$ m, is only 2.3 m; 3.7 m less than for $x > 800$ m equating to a 37 m difference in thickness. Over the 800 m region considered here, the total loss of ice necessary to cause this difference in mélange height can be approximated as the difference in thickness from the other regions. This suggests that, on average, between 38 and 45 m of ice has been removed from this area of the mélange by the plume.

3.5. Plume Modeling

3.5.1. Modeled Surface Elevation

The characteristic surface elevations extracted from the plume model for the two terminus depths tested are shown in Figure 7, this can also be compared to the melt rate plots in Figure S3. At a discharge of 10 $\mathrm{m^3\,s^{-1}}$ neither plume had a significant effect on the surface, with the characteristic surface heights at both terminus depths only around 0.01 m above sea level. As the discharge increases to 100 $\mathrm{m^3\,s^{-1}}$ the surface height begins to increase, with heights of 0.04 and 0.09 m for the 700 and 500 m deep terminus respectively. As the discharge increases above 100 $\mathrm{m^3\,s^{-1}}$ the plume surface height increases nonlinearly, showing a rapid increase at lower discharges which begins to plateau at higher discharges. In the range of discharges tested, the 700 m deep terminus reached a maximum surface height of 0.45 m at a discharge of 1,000 $\mathrm{m^3\,s^{-1}}$, and the 500 m deep terminus reached a maximum of 0.76 m at the same discharge. At all discharges, the surface heights driven by the plume with a 500 m deep terminus are consistently higher than those for a 700 m deep terminus at the same discharge volume. The results demonstrate that, in the absence of mélange, the plumes will become visible on the surface for discharges between 10 and 100 $\mathrm{m^3\,s^{-1}}$, and at discharges above 100 $\mathrm{m^3\,s^{-1}}$ the plume will likely to be clearly visible on the surface irrespective of the terminus depth.

3.5.2. Modeled Melt Rates

Modeled melt rates for a range of discharges are shown in Figure S4. The maximum modeled integrated melt rate was 236.5×10^3 $\mathrm{m^3\,d^{-1}}$ for a discharge of 1,000 $\mathrm{m^3\,s^{-1}}$ and the lowest was 55×10^3 $\mathrm{m^3\,d^{-1}}$ for a discharge of 10 $\mathrm{m^3\,s^{-1}}$. As found by Slater et al. (2015), modeled melt did not increase linearly with discharge. Across the range of discharges tested here, an increase of two orders of magnitude in subglacial discharge volume led to a four-fold increase in melt volume. In these results, the melt rate scaled approximately with the fourth root of discharge.

The results show that discharge volumes below 100 $\mathrm{m^3\,s^{-1}}$ had a negligible effect on the melt rate directly at the ocean surface; however, plume-driven melt did reach within 100 m of the surface and therefore could contribute to undercutting of the terminus above. At higher discharges, the maximum melt rate driven by the plume was closer to the surface. At 300 $\mathrm{m^3\,s^{-1}}$, the maximum melt was around 200 m above the source, while at 1,000 $\mathrm{m^3\,s^{-1}}$ the maximum melt rate was around 400 m above the source. Thus higher discharges will have a greater impact on surface undercutting than the increase in discharge alone. A feature visible in most cases, and particularly at high discharges, is the reduction in melt rate just below the surface. This feature is driven by the transition of the plume from vertical to horizontal flow; where the minimum in melt rate marks the lowest absolute velocity as the plume decelerates in the vertical and accelerates in the horizontal. Therefore, while the majority of the melting on the terminus is driven by high vertical velocities, immediately at the surface the high melt rates are driven by the horizontal export of water away from the plume.

4. Discussion

4.1. Estimating Discharge in the Plume

Using Figure 7 it is possible to infer what discharge would be required at each terminus depth to produce the characteristic surface height observed in the LiDAR data. For a 500 m deep terminus, the discharge required to produce the surface expression observed in the LiDAR data is $353^{+32}_{-27}\,\mathrm{m^3\,s^{-1}}$, while for a 700 m deep terminus the required discharge is considerably higher at $729^{+271}_{-197}\,\mathrm{m^3\,s^{-1}}$. There is a much greater uncertainty in the discharge for the 700 m deep terminus, as the characteristic surface height appears to approach a maximum for that terminus depth.

The discharge estimates can be compared to Mernild et al. (2010) who used a distributed snow-evolution modeling system (SnowModel) (Liston & Elder, 2006) with in situ meteorological data to estimate that the mean volume of runoff released from Helheim catchment between 1999 and 2008 was $1.0 \pm 0.2 \times 10^9\,\mathrm{m^3\,yr^{-1}}$. This volume varied from $0.7 \pm 0.1 \times 10^9\,\mathrm{m^3\,yr^{-1}}$ in 1999 and 2003 to $1.3 \pm 0.2 \times 10^9\,\mathrm{m^3\,yr^{-1}}$ in 2005 and 2007. From the plume record, the plume was visible at the terminus for 21 days in 2013. If it is assumed that the mean discharge calculated by Mernild et al. (2010) was released entirely within this 21-day period, this would give a time-averaged discharge of $551 \pm 110\,\mathrm{m^3\,s^{-1}}$ with a minimum of $386 \pm 55\,\mathrm{m^3\,s^{-1}}$ in the lowest discharge years (1999, 2003) and a maximum of $716 \pm 110\,\mathrm{m^3\,s^{-1}}$ in the highest discharge years (2005, 2007). The runoff estimates do not cover the same time period, but the discharge estimates from the 500 and 700 m deep terminus model runs cover a similar range to the interannual variability of the runoff estimates of Mernild et al. (2010).

The surface expression of the plume captured by the LiDAR is an instantaneous measurement of a surface which will change rapidly as turbulent eddies in the plume reach the surface. Ideally, multiple surface profiles would be collected and the time-averaged characteristic surface height would be extracted using an identical method to the plume model. However, this is an opportunistic use of a coincidental LiDAR acquisition over a plume and is currently the only one known to have been collected. The methods and estimates presented here show that further collection of such data would allow direct comparison to model results, and should allow these estimates to be constrained further.

4.2. Direct Plume-Driven Mass Loss

For this discussion, we split the direct effects of the plume on mass loss into two components: i) submarine melting as the plume rises up the terminus, which can currently only be approximated from model results, and ii) retreat of the subaerial section of the terminus, which can be derived from the observations. The plume may also have indirect effects on mass loss through an amplification of the size or frequency of large calving events. This is discussed in the next section.

4.2.1. Submarine Melting

The estimates presented in this paper have shown the plume discharge to be in the region of $400\,\mathrm{m^3\,s^{-1}}$. The model results show that this volume of discharge would drive a total daily mass loss of $216 \times 10^3\,\mathrm{m^3\,d^{-1}}$ of ice from the terminus. The lower limit of the discharge estimate based upon the terminus retreat rate is a discharge of $100\,\mathrm{m^3\,s^{-1}}$, which would drive a total daily mass loss of $127 \times 10^3\,\mathrm{m^3\,d^{-1}}$. From the complete years in the plume record, the plume was present at the terminus for between 14 (2014) and 33 (2012) days. Taking the upper limit of 33 days and a discharge of $400\,\mathrm{m^3\,s^{-1}}$, the total plume-driven mass loss in a year can be estimated as $7.1 \times 10^6\,\mathrm{m^3\,yr^{-1}}$. For comparison, a single calving event at Helheim Glacier observed by Murray et al. (2015a) removed $360 \times 10^6\,\mathrm{m^3}$ of ice from the terminus. This suggests that a single calving event removes two orders of magnitude more ice than plume-driven melting does throughout the melt season.

There is a large amount of uncertainty in the plume-driven mass loss estimate. These uncertainties are due to a range of factors including uncertainties in the volume of discharge released from the terminus, the time

the plume was present, whether the plume reached the surface and the three-equation melt parameterization used to derive the melt in the plume model. However, none of these are likely to account for a two orders of magnitude error in the melt rate. Uncertainties in discharge could not explain these differences due to the fourth-root dependency of melt on discharge; implying that increasing the volume of discharge makes only a small difference to the modeled melt estimate. Our observations may underestimate the time the plume was present if, for example, the plume did not reach the surface or was obscured by the mélange. However, even taking an extreme scenario where the plume was present every day of the year, this would only increase the total annual plume-driven submarine melt to 79×10^6 m^3, still an order of magnitude smaller than a single calving event. Thus increasing the time which the plume was present at the terminus would also not allow the plume to reach melt rates comparable to the mass loss through calving.

An alternative way that plumes can lead to increased melting is if discharge is released through a distributed subglacial system, as demonstrated by Slater et al. (2015). A distributed system leads to a higher number of smaller plumes, but the net effect is to increase mass loss from the terminus when compared to a single plume. While the evidence collected in this paper only supports the presence of a single plume at Helheim, without further observations we cannot rule out the presence of a background, distributed release of subglacial discharge or other plumes which do not reach the surface. In an extreme case of 40 individual plumes each releasing 10 m^{3}s^{-1} of discharge, the model results presented here show that mass loss due to each individual plume would be 55×10^3 m^{3}d^{-1}. To match the mass loss from a single calving event, these 40 plumes would have to be active for more than 150 days during the melt season. This would require an annual discharge of 5.2×10^9 m^{3}yr^{-1}, five times the highest runoff estimates of Mernild et al. (2010).

The plume model used here also considers only a relatively narrow domain and, as demonstrated by Slater et al. (2018), plumes can set up a wider circulation in front of the glacier which can lead to a wider-scale enhancement of submarine melting and increased estuarine circulation. Slater et al. (2018) find that the integrated mass loss due to this circulation is approximately double that of the plume, leading to annual melt rates of around 100 m^{3}yr^{-1} which is not accounted for in the model results presented here. However, as previously highlighted, a single major calving event can remove up to 500 m of ice from the terminus of the glacier. Therefore, even when accounting for this, plume-driven mass loss appears to be much smaller than that due to calving at Helheim Glacier.

4.2.2. Undercutting and Collapse

While we must rely on modeled melt rates to estimate submarine melting, the observations presented in this paper provide useful estimates of the surface retreat rates driven by the plume. The volume of ice lost by the formation of the embayment is $\sim 3.0 \times 10^6$ m^3 over a period of 16 days. This suggests an average loss of 188×10^3 m^{3}d^{-1}. As with submarine melting, this is many orders of magnitude smaller than a typical calving event at Helheim Glacier. Based on these estimates, even if the plume was present at Helheim Glacier every day for a year, it would only lead to the loss of around 70×10^6 m^3 of ice through plume-induced calving, which is still less than one fifth of the ice lost in a single calving event. Therefore, as with plume-driven submarine melt, plume-driven undercutting seems unlikely to have a significant impact on the terminus when compared to calving events at Helheim Glacier.

Given these considerations, our results suggest that direct mass loss driven by the plume at Helheim, whether by submarine melting or undercutting and collapse, is significantly lower than that resulting from major calving events driven by other processes at the glacier (e.g., James et al., 2014; Joughin et al., 2008; Kehrl et al., 2017). The currently limited data makes it difficult to quantify this exactly; however, the estimated mass loss driven by the plume observed in 2013 indicates that direct plume-driven mass loss is at least one order of magnitude less than calving.

4.2.3. Comparison Between Modeled and Observed Surface Retreat

The surface retreat observed in the hyperspectral image can be directly compared to the modeled surface melting from the plume model. This comparison is shown in Figure 8. The comparison shows that the modeled and observed profiles have similar magnitudes, but the observed profile demonstrate much wider spreading of melting than the model.
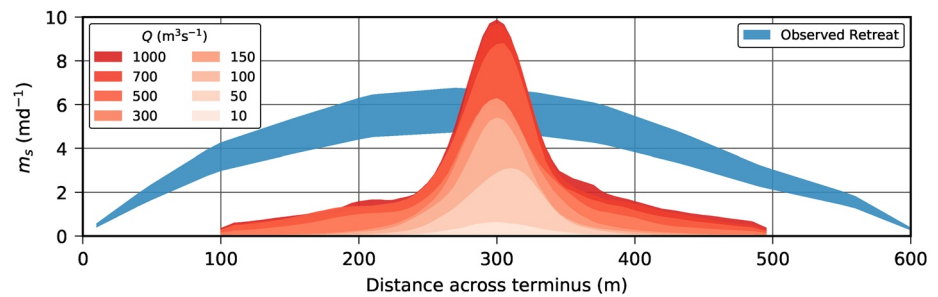
Figure 8. Modeled surface retreat profiles for a range of discharges compared to the observed range of surface retreat (blue shading).

The difference cannot be explained simply by the model not capturing plume dynamics correctly. Plume dynamics in idealized scenarios are well tested against observations (e.g., Hunt & van den Bremer, 2011; Morton et al., 1956), including the ability of the model to capture entrainment and spreading processes. The differences observed here are therefore likely due to the nonidealized geometry of plumes at glacier termini, which also evolves during the lifetime of the plume. This is something which current plume models are unable to capture, and therefore highlights an area for future development of these models. It is impossible to tell from the observational data available whether this wider spreading is a surface effect as the plume impinges on the ocean surface and spreads laterally, or whether it may affect the full depth of the terminus.

If this underestimate of melting in the plume model were to affect the full depth of the terminus, the plume model would be underestimating melt by a factor of between two and three. Even accounting for this, the mass loss driven by the plume is still many times smaller than a single major calving event.

4.3. Impacts of the Plume on the Mélange

From the results it is possible to make some inferences about the appearance of the plume through the mélange. There is no evidence of pile-up around the edges of the plume opening, which might imply that the opening was cleared by the horizontal motion of the plume as it leaves the ice front. Given the size of the icebergs within the mélange around the edge of the plume, some greater than 20 m thick, it seems unlikely the surface velocities would be significant enough to pile up icebergs of this size. The absence of this buildup of ice suggests that the opening was cleared by plume-driven melting, though we cannot determine this conclusively from the data collected here.

Using the method described in Section 2.4.2, the mélange was calculated to be 60 m thick on average. Therefore, assuming that the melt rate in the mélange is roughly equivalent to the surface melt rate of the plume on the vertical ice face, that is, ~4 m day^{-1}, it could take up to 15 days for the plume to become visible on the surface. It is also worth considering that during this time ice will continuously be added to the mélange due to undercutting and collapse of the subaerial section of the terminus, which may further delay the appearance of the plume. This is a significant delay, and suggests that some allowance must be made that the plume record derived in this study is an underestimate.

Once the plume has created an opening in the mélange, the melt rate necessary to maintain the opening would be significantly lower than that necessary to create it. For example, taking numbers from the data; the mélange opening is 36.5×10^3 m^2 and stretches across 230 m of the terminus which is around 70 m high. The mean retreat rate of the terminus across the embayment determined from observations is 4.4 m day^{-1}; assuming that this retreat rate can be applied to the full height of the terminus above the water and across the width of the embayment, this suggests that around 71×10^3 m^3 day^{-1} of ice will be added to the opening. Assuming this ice is distributed evenly across the opening, the melt rate only needs to be ~2 m day^{-1} in order to melt this added ice and therefore to maintain or increase the size of the opening.

These considerations suggest that the primary driver for clearing the mélange is through melting driven by the plume. The results also clearly illustrate that measuring the size of the opening in the mélange could be very misleading for estimating the melt rates and discharges within the plume, and would strongly depend

on how long the plume had been active. Perhaps a more useful measure could be gained from a time series of plume area, in order to observe how quickly the area grew or shrank; however, this would also require a reasonably accurate measure of the rate of input of ice from the terminus.

It is clear from the LiDAR swath that the plume affects melting of the mélange over a much wider area than the visible opening. Figure 5 shows that the mélange is thinned, and presumably therefore weakened, over a width of 800 m across the terminus. The influence of the mélange on calving is debated (Amundson et al., 2010; Cook et al., 2014); however, the discussion in the previous section regarding the timing of the plume and calving events would also apply here. If the weakened mélange did have an impact on calving, we would expect to see calving events preceded closely by plumes. The delay of many days after the plume ceases to surface would allow time for the opening in the mélange to close, especially given that Helheim is moving forward tens of meters per day, which will quickly compress the mélange. Thus, the results presented here suggest the observed weakening of the mélange by the plume does not have a direct influence on calving.

4.4. Plume Relation to Major Calving Events at Helheim

Undercutting by submarine melting has been shown to have a complex effect on major calving events. In the case of uniform undercutting across a glacier terminus, the size and frequency of calving events can increase (O'Leary & Christoffersen, 2013), but in other situations modeling studies have shown that submarine melting can suppress calving (Benn et al., 2017; Ma & Bassis, 2019). A major consideration at Helheim is the limited width of the plume observed here in relation to the width and depth of the terminus. This may limit the impacts on the near-terminus stress field investigated by (O'Leary & Christoffersen, 2013) and therefore the ability to amplify calving in this way.

We can also consider the timing of the calving events in relation to the plume. In most of the years studied here there is no consistent pattern of major calving events quickly following plume activity on the surface, which might be expected if the plume was having a significant effect on calving. The only year when such behavior may be evident is in 2012; however, this appears to be the exception rather than the norm, and could be coincidental in a single year.

The results presented in this study show instead that the surface presence of a plume at Helheim is associated with longer delays between calving events and that this relationship is significant. Given that the buoyant flexure calving mechanism is known to occur at Helheim Glacier (Wagner et al., 2016), this may be explained by submarine melting by the plume leading to a reduction in buoyancy at the terminus. Such a mechanism has been demonstrated in modeling studies (Benn et al., 2017; Ma & Bassis, 2019), and the observations here appear to confirm the existence of this mechanism affecting calving at Helheim.

A second possibility is that the observed delays in plume activity following calving are due to an interruption of the plume's activity by the calving event. This could be through alterations of the hydrological system during calving events. Such an interruption could be caused by the formation of new basal crevasses or due to changes at the bed caused by rapid changes in glacier flow speed which have been observed before, during and after calving events (Murray et al., 2015b). Alternatively, the addition of ice to the mélange could also delay the return of the plume. The previous section demonstrated the significant length of time which may be required for a plume to clear an opening in the mélange. However, there are numerous cases in the record of the plume returning within one or two days of calving. Therefore, even if this interruption occurs in some cases, it cannot fully explain the significant difference in the delay between calving events.

Finally, the plume is typically only present at the surface on two to five occasions per year. A number of these occurrences are for two to three days, which would give very limited opportunity for the melt rates to have a significant impact on the terminus. This means that the plume only has the potential to influence a small number of major calving events per year. The plume and calving record shows many more individual calving events than there are occurrences of a plume at the terminus. The evidence collected here, though not conclusive, strongly suggests that mass loss driven directly by the plume is of lesser importance than the internal dynamics of the glacier in determining the size and frequency of calving events at Helheim Glacier. However, we emphasize that this observation most likely only applies to wide and deep glacier termini, and would not be applicable to shallower termini which are characterized by very different calving behavior.

5. Conclusions

We have presented a detailed modeling and observational study of a plume of subglacial discharge at the terminus of Helheim Glacier, south east Greenland, and its relation to calving events. The results presented show that Helheim Glacier is characterized by a single source of subglacial discharge. While we cannot rule out background/distributed releases, we have found no evidence for this. We used LiDAR profiles of a surface bulge to estimate discharge in the observed plume, and showed that these estimates are consistent with independently derived runoff estimates. Thus suggesting that any background distributed discharges in addition to the main plume, if existent, would have to be small.

This study has demonstrated how an opportunistic use of LiDAR data collected over the surface of a plume can be used to further refine modeling efforts. Targeted and repeated use of this method in future could significantly improve our ability to monitor these plumes and constrain the volume of subglacial discharge they contain. However, our study has also highlighted disagreement between plume models and observations, particularly in the retreat rate of the glacier in the plume embayment. This deficiency is an important area which must be addressed if future modeling efforts are to produce reliable results.

Consistent with modeling studies, we have shown that plumes can be associated with longer delays between calving events. Furthermore, our estimates of mass loss driven by the plume, including undercutting and collapse, are small relative to mass loss by calving. These estimates are subject to many uncertainties; however, it is difficult to reconcile the order of magnitude differences between plume-driven melt and a single major calving event at Helheim, particularly as our observational results show that between four and ten of these events occur each year. A number of studies have found links between ocean temperature and mass loss at Greenlandic glaciers (Holland et al. (2008); Khazendar et al. (2019)). Plumes of subglacial discharge have been widely implicated in this mass loss and, while our results do not dispute their involvement, we have shown that their direct effects on calving and mass loss at large Greenlandic glaciers may be smaller than currently thought. This highlights the importance of understanding the processes linking ocean temperature changes and their relative contributions to mass loss. Our results are likely specific to large and deep marine-terminating glaciers, but are therefore particularly important for understanding future changes at large marine terminating glaciers around the Greenland ice sheet.

Data Availability Statement

Hyperspectral and Lidar data from flight IG13/21 are available at http://data.ceda.ac.uk/neodc/arsf/2013/IG13_21/IG13_21-2013_198_Helheim. Camera images are available at https://doi.org/10.5281/zenodo.3461071. Fluidity is an opensource software package available from https://fluidityproject.github.io/.

References

AMCG, I. C. L. (2015). *Fluidity manual v4.1.12*. https://doi.org/10.6084/m9.figshare.1387713.v2

Amundson, J. M., Fahnestock, M., Truffer, M., Brown, J., Lüthi, M. P., & Motyka, R. J. (2010). Ice melange dynamics and implications for terminus stability, Jakobshavn Isbræ, Greenland. *Journal of Geophysical Research*, 115, F01005. https://doi.org/10.1029/2009JF001405

Bartholomaus, T. C., Amundson, J. M., Walter, J. I., O'Neel, S., West, M. E., & Larsen, C. F. (2015). Subglacial discharge at tidewater glaciers revealed by seismic tremor. *Geophysical Research Letters*, 42(15), 6391–6398. https://doi.org/10.1002/2015gl064590

Benn, D. I., Jan, Å., Zwinger, T., Todd, J., Nick, F. M., Cook, S., et al. (2017). Melt-under-cutting and buoyancy-driven calving from tidewater glaciers: New insights from discrete element and continuum model simulations. *Journal of Glaciology*, 63(240), 691–702. https://doi.org/10.1017/jog.2017.41

Benn, D. I., Warren, C. R., & Mottram, R. H. (2007). Calving processes and the dynamics of calving glaciers. *Earth-Science Reviews*, 82(3–4), 143–179. https://doi.org/10.1016/j.earscirev.2007.02.002

Bull, J. R., Piggott, M. D., & Pain, C. C. (2012). *A finite element LES methodology for anisotropic inhomogeneous meshes*. Proceedings of the Seventh International Symposium on Turbulence, Heat and Mass Transfer Palermo, Italy, 24–27 September, 2012. https://doi.org/10.1615/ichmt.2012.procsevintsympturbheattransfpal.1560

Carroll, D., Sutherland, D. A., Hudson, B., Moon, T., Catania, G. A., Shroyer, E. L., et al. (2016). The impact of glacier geometry on meltwater plume structure and submarine melt in Greenland fjords. *Geophysical Research Letters*, 43(18), 9739–9748. https://doi.org/10.1002/2016gl070170

Carroll, D., Sutherland, D. A., Shroyer, E. L., Nash, J. D., Catania, G. A., & Stearns, L. A. (2015). Modeling turbulent subglacial meltwater plumes: Implications for fjord-scale buoyancy-driven circulation. *Journal of Physical Oceanography*, 45(8), 2169–2185. https://doi.org/10.1175/jpo-d-15-0033.1

Church, J., Clark, P., Cazenave, A., Gregory, J., Jevrejeva, S., Levermann, A., et al. (2013). *Sea level change*. Cambridge University Press. https://doi.org/10.1017/CBO9781107415324.026

Cook, S., Rutt, I. C., Murray, T., Luckman, A., Zwinger, T., Selmes, N., et al. (2014). Modelling environmental influences on calving at Helheim Glacier in eastern Greenland. *The Cryosphere*, *8*(3), 827–841. https://doi.org/10.5194/tc-8-827-2014

Davies, D. R., Wilson, C. R., & Kramer, S. C. (2011). Fluidity: A fully unstructured anisotropic adaptive mesh computational modeling framework for geodynamics. *Geochemistry, Geophysics, Geosystems*, *12*, Q06001. https://doi.org/10.1029/2011gc003551

Enderlin, E. M., Howat, I. M., Jeong, S., Noh, M.-J., van Angelen, J. H., & van den Broeke, M. R. (2014). An improved mass budget for the Greenland ice sheet. *Geophysical Research Letters*, *41*(3), 866–872. https://doi.org/10.1002/2013gl059010

Everett, A., Murray, T., Selmes, N., Rutt, I. C., Luckman, A., James, T. D., et al. (2016). Annual down-glacier drainage of lakes and water-filled crevasses at Helheim Glacier, south east Greenland. *Journal of Geophysical Research: Earth Surface*, *121*(10), 1819–1833. https://doi.org/10.1002/2016jf003831

Holland, D. M., & Jenkins, A. (1999). Modeling thermodynamic ice-ocean interactions at the base of an ice shelf. *Journal of Physical Oceanography*, *29*, 1787–1800.

Holland, D. M., Thomas, R. H., de Young, B., Ribergaard, M. H., & Lyberth, B. (2008). Acceleration of Jakobshavn Isbrae triggered by warm subsurface ocean waters. *Nature Geoscience*, *1*(10), 659–664. https://doi.org/10.1038/ngeo316

How, P., Benn, D. I., Hulton, N. R. J., Hubbard, B., Luckman, A., Sevestre, H., et al. (2017). Rapidly changing subglacial hydrological pathways at a tidewater glacier revealed through simultaneous observations of water pressure, supraglacial lakes, meltwater plumes and surface velocities. *The Cryosphere*, *11*(6), 2691–2710. https://doi.org/10.5194/tc-11-2691-2017

How, P., Schild, K. M., Benn, D. I., Noormets, R., Kirchner, N., Luckman, A., et al. (2019). Calving controlled by melt-under-cutting: Detailed calving styles revealed through time-lapse observations. *Annals of Glaciology*, *60*(78), 20–31. https://doi.org/10.1017/aog.2018.28

Hunt, G. R., & van den Bremer, T. S. (2011). Classical plume theory: 1937–2010 and beyond. *IMA Journal of Applied Mathematics*, *76*(3), 424–448. https://doi.org/10.1093/imamat/hxq056

Jackson, R. H., Shroyer, E. L., Nash, J. D., Sutherland, D. A., Carroll, D., Fried, M. J., et al. (2017). Near-glacier surveying of a subglacial discharge plume: Implications for plume parameterizations. *Geophysical Research Letters*, *44*(13), 6886–6894. https://doi.org/10.1002/2017gl073602

James, T. D., Murray, T., Selmes, N., Scharrer, K., & O'Leary, M. (2014). Buoyant flexure and basal crevassing in dynamic mass loss at Helheim Glacier. *Nature Geoscience*, *7*(8), 593–596. https://doi.org/10.1038/ngeo2204

Jarrin, N., Benhamadouche, S., Laurence, D., & Prosser, R. (2006). A synthetic-eddy-method for generating inflow conditions for large-eddy simulations. *International Journal of Heat and Fluid Flow*, *27*(4), 585–593. https://doi.org/10.1016/j.ijheatfluidflow.2006.02.006

Jenkins, A. (2011). Convection-driven melting near the grounding lines of ice shelves and tidewater glaciers. *Journal of Physical Oceanography*, *41*(12), 2279–2294. https://doi.org/10.1175/JPO-D-11-03.1

Joughin, I., Howat, I., Alley, R. B., Ekstrom, G., Fahnestock, M., Moon, T., et al. (2008). Ice-front variation and tidewater behavior on Helheim and Kangerdlugssuaq Glaciers, Greenland. *Journal of Geophysical Research*, *113*, F01004. https://doi.org/10.1029/2007JF000837

Keating, A., Piomelli, U., Balaras, E., & Kaltenbach, H.-J. (2004). A priori and a posteriori tests of inflow conditions for large-eddy simulation. *Physics of Fluids*, *16*(12), 4696. https://doi.org/10.1063/1.1811672

Kehrl, L. M., Joughin, I., Shean, D. E., Floricioiu, D., & Krieger, L. (2017). Seasonal and interannual variability in terminus position, glacier velocity, and surface elevation at Helheim and Kangerlussuaq Glaciers from 2008 to 2016. *Journal of Geophysical Research: Earth Surface*, *122*, 1635–1652. https://doi.org/10.1002/2016jf004133

Khazendar, A., Fenty, I. G., Carroll, D., Gardner, A., Lee, C. M., Fukumori, I., et al. (2019). Interruption of two decades of Jakobshavn Isbrae acceleration and thinning as regional ocean cools. *Nature Geoscience*, *12*(4), 277–283. https://doi.org/10.1038/s41561-019-0329-3

Kimura, S., Candy, A. S., Holland, P. R., Piggott, M. D., & Jenkins, A. (2013). Adaptation of an unstructured-mesh, finite-element ocean model to the simulation of ocean circulation beneath ice shelves. *Ocean Modelling*, *67*, 39–51. https://doi.org/10.1016/j.ocemod.2013.03.004

Kimura, S., Holland, P. R., Jenkins, A., & Piggott, M. (2014). The effect of meltwater plumes on the melting of a vertical glacier face. *Journal of Physical Oceanography*, *44*, 3099–3177. https://doi.org/10.1175/jpo-d-13-0219.1

Liston, G. E., & Elder, K. (2006). A distributed snow-evolution modeling system (SnowModel). *Journal of Hydrometeorology*, *7*(6), 1259–1276. https://doi.org/10.1175/jhm548.1

Ma, Y., & Bassis, J. N. (2019). The effect of submarine melting on calving from marine terminating glaciers. *Journal of Geophysical Research: Earth Surface*, *124*, 334–346. https://doi.org/10.1029/2018jf004820

Mankoff, K. D., Straneo, F., Cenedese, C., Das, S. B., Richards, C. G., & Singh, H. (2016). Structure and dynamics of a subglacial discharge plume in a Greenlandic fjord. *Journal of Geophysical Research: Oceans*, *121*(12), 8670–8688. https://doi.org/10.1002/2016jc011764

McConnochie, C. D., & Kerr, R. C. (2017). Testing a common ice-ocean parameterization with laboratory experiments. *Journal of Geophysical Research: Oceans*, *122*(7), 5905–5915. https://doi.org/10.1002/2017jc012918

McDougall, T. J., Jackett, D. R., Wright, D. G., & Feistel, R. (2003). Accurate and computationally efficient algorithms for potential temperature and density of seawater. *Journal of Atmospheric and Oceanic Technology*, *20*(5), 730–741. https://doi.org/10.1175/1520-0426(2003)20¡730:aaceaf¿2.0.co;2

Mernild, S. H., Howat, I. M., Ahn, Y., Liston, G. E., Steffen, K., Jakobsen, B. H., et al. (2010). Freshwater flux to Sermilik Fjord, SE Greenland. *The Cryosphere*, *4*(4), 453–465. https://doi.org/10.5194/tc-4-453-2010

Morton, B. R., Taylor, G., & Turner, J. S. (1956). Turbulent gravitational convection from maintained and instantaneous sources. *Proceedings of the Royal Society A: Mathematical, Physical & Engineering Sciences*, *234*(1196), 1–23. https://doi.org/10.1098/rspa.1956.0011

Motyka, R. J., Dryer, W. P., Amundson, J., Truffer, M., & Fahnestock, M. (2013). Rapid submarine melting driven by subglacial discharge, LeConte Glacier, Alaska. *Geophysical Research Letters*, *40*(19), 5153–5158. https://doi.org/10.1002/grl.51011

Murray, T., Nettles, M., Selmes, N., Cathles, L. M., Burton, J. C., James, T. D., et al. (2015a). Reverse glacier motion during iceberg calving and the cause of glacial earthquakes. *Science*, *349*(6245), 305–308. https://doi.org/10.1126/science.aab0460

Murray, T., Selmes, N., James, T. D., Edwards, S., Martin, I., O'Farrell, T., et al. (2015b). Dynamics of glacier calving at the ungrounded margin of Helheim Glacier, southeast Greenland. *Journal of Geophysical Research: Earth Surface*, *120*(6), 964–982. https://doi.org/10.1002/2015jf003531

Olsen, K. G., & Nettles, M. (2017). Patterns in glacial-earthquake activity around Greenland, 2011–13. *Journal of Glaciology*, *63*(242), 1077–1089. https://doi.org/10.1017/jog.2017.78

O'Leary, M., & Christoffersen, P. (2013). Calving on tidewater glaciers amplified by submarine frontal melting. *The Cryosphere*, *7*(1), 119–128. https://doi.org/10.5194/tc-7-119-2013

Piggott, M. D., Gorman, G. J., Pain, C. C., Allison, P. A., Candy, A. S., Martin, B. T., & Wells, M. R. (2008). A new computational framework for multi-scale ocean modeling based on adapting unstructured meshes. *International Journal for Numerical Methods in Fluids*, *56*(8), 1003–1015. https://doi.org/10.1002/fld.1663

Schild, K. M., Hawley, R. L., & Morriss, B. F. (2016). Subglacial hydrology at Rink Isbræ, West Greenland inferred from sediment plume appearance. *Annals of Glaciology*, *57*(72), 118–127. https://doi.org/10.1017/aog.2016.1

Schoof, C. (2010). Ice-sheet acceleration driven by melt supply variability. *Nature*, *468*(7325), 803–806. https://doi.org/10.1038/nature09618

Slater, D. A., Goldberg, D. N., Nienow, P. W., & Cowton, T. R. (2016). Scalings for submarine melting at tidewater glaciers from buoyant plume theory. *Journal of Physical Oceanography*, *46*(6), 1839–1855. https://doi.org/10.1175/jpo-d-15-0132.1

Slater, D. A., Nienow, P. W., Cowton, T. R., Goldberg, D. N., & Sole, A. J. (2015). Effect of near-terminus subglacial hydrology on tidewater glacier submarine melt rates. *Geophysical Research Letters*, *42*, 2861–2868. https://doi.org/10.1002/2014gl062494

Slater, D. A., Nienow, P., Sole, A., Cowton, T., Mottram, R., Langen, P., & Mair, D. (2017a). Spatially distributed runoff at the grounding line of a large Greenlandic tidewater glacier inferred from plume modeling. *Journal of Glaciology*, *63*(238), 309–323. https://doi.org/10.1017/jog.2016.139

Slater, D. A., Nienow, P. W., Goldberg, D. N., Cowton, T. R., & Sole, A. J. (2017b). A model for tidewater glacier undercutting by submarine melting. *Geophysical Research Letters*, *44*, 2360–2368. https://doi.org/10.1002/2016gl072374

Slater, D. A., Straneo, F., Das, S. B., Richards, C. G., Wagner, T. J. W., & Nienow, P. W. (2018). Localized plumes drive front-wide ocean melting of a Greenlandic tidewater glacier. *Geophysical Research Letters*, *45*(22), 12350–12358. https://doi.org/10.1029/2018GL080763

Smagorinsky, J. (1963). General circulation experiments with the primitive equations. *Monthly Weather Review*, *91*(3), 99–164. https://doi.org/10.1175/1520-0493(1963)091<0099:gcewtp>2.3.co;2

Straneo, F., & Cenedese, C. (2015). The dynamics of Greenland's glacial fjords and their role in climate. *Annual Review of Marine Science*, *7*(1), 89–112. https://doi.org/10.1146/annurev-marine-010213-135133

Straneo, F., & Heimbach, P. (2013). North Atlantic warming and the retreat of Greenland's outlet glaciers. *Nature*, *504*(7478), 36–43. https://doi.org/10.1038/nature12854

Sutherland, D. A., Jackson, R. H., Kienholz, C., Amundson, J. M., Dryer, W. P., Duncan, D., et al. (2019). Direct observations of submarine melt and subsurface geometry at a tidewater glacier. *Science*, *365*(6451), 369–374. https://doi.org/10.1126/science.aax3528

Tsai, V. C., & Ekström, G. (2007). Analysis of glacial earthquakes. *Journal of Geophysical Research*, *112*, F03S22. https://doi.org/10.1029/2006jf000596

Veitch, S. A., & Nettles, M. (2012). Spatial and temporal variations in Greenland glacial-earthquake activity, 1993–2010. *Journal of Geophysical Research*, *117*, F04007. https://doi.org/10.1029/2012jf002412

Wagner, T. J. W., James, T. D., Murray, T., & Vella, D. (2016). On the role of buoyant flexure in glacier calving. *Geophysical Research Letters*, *43*(1), 232–240. https://doi.org/10.1002/2015gl067247

Xu, Y., Rignot, E., Fenty, I., Menemenlis, D., & Mar Flexas, M. (2013). Subaqueous melting of Store Glacier, West Greenland from three-dimensional, high-resolution numerical modeling and ocean observations. *Geophysical Research Letters*, *40*(17), 4648–4653. https://doi.org/10.1002/grl.50825

Reference From the Supporting Information

Jenkins, A., Nicholls, K. W., & Corr, H. F. J. (2010). Observation and parameterization of ablation at the base of Ronne Ice Shelf, Antarctica. *Journal of Physical Oceanography*, *40*(10), 2298–2312. https://doi.org/10.1175/2010JPO4317.1